The polarization observables T, P, and H and their impact on $\gamma p \to p\pi^0$ multipoles

J. Hartmann[a], H. Dutz[b], A.V. Anisovich[a,c], D. Bayadilov[a,c], R. Beck[a], M. Becker[a], Y. Beloglazov[c], A. Berlin[d], M. Bichow[d], S. Böse[a], K.-Th. Brinkmann[e,a], V. Crede[f], M. Dieterle[g], H. Eberhardt[b], D. Elsner[b], K. Fornet-Ponse[b], St. Friedrich[e], F. Frommberger[b], Ch. Funke[a], M. Gottschall[a], A. Gridnev[c], M. Grüner[a], St. Görtz[b], E. Gutz[e,a], Ch. Hammann[a], J. Hannappel[b], V. Hannen[e], J. Herick[d], W. Hillert[b], Ph. Hoffmeister[a], Ch. Honisch[a], O. Jahn[b], T. Jude[b], A. Käser[g], D. Kaiser[a], H. Kalinowsky[a], F. Kalischewski[a], P. Klassen[a], I. Keshelashvili[g], F. Klein[b], E. Klempt[a], K. Koop[a], B. Krusche[g], M. Kube[a], M. Lang[a], I. Lopatin[c], K. Makonyi[e], F. Messi[b], V. Metag[e], W. Meyer[d], J. Müller[a], M. Nanova[e], V. Nikonov[a,c], D. Novinski[c], R. Novotny[e], D. Piontek[a], S. Reeve[b], Ch. Rosenbaum[a], B. Roth[d], G. Reicherz[d], T. Rostomyan[g], St. Runkel[b], A. Sarantsev[a,c], Ch. Schmidt[a], H. Schmieden[b], R. Schmitz[a], T. Seifen[a], V. Sokhoyan[a], Ph. Thämer[a], A. Thiel[a], U. Thoma[a], M. Urban[a], H. van Pee[a], D. Walther[a], Ch. Wendel[a], U. Wiedner[d], A. Wilson[a,f], A. Winnebeck[a], L. Witthauer[g],

CBELSA/TAPS Collaboration

[a]*Helmholtz–Institut für Strahlen– und Kernphysik, Universität Bonn, 53115 Bonn, Germany*
[b]*Physikalisches Institut, Universität Bonn, 53115 Bonn, Germany*
[c]*Petersburg Nuclear Physics Institute, Gatchina, 188300 Russia*
[d]*Institut für Experimentalphysik I, Ruhr–Universität Bochum, 44780 Bochum, Germany*
[e]*II. Physikalisches Institut, Universität Gießen, 35392 Gießen, Germany*
[f]*Department of Physics, Florida State University, Tallahassee, Florida 32306, USA*
[g]*Department Physik, Universität Basel, 4056 Basel, Switzerland*

Abstract

Data on the polarization observables T, P, and H for the reaction $\gamma p \to p\pi^0$ are reported. Compared to earlier data from other experiments, our data are more precise and extend the covered range in energy and angle substantially. The results were extracted from azimuthal asymmetries measured using a transversely polarized target and linearly polarized photons. The data were taken at the Bonn electron stretcher accelerator ELSA with the CBELSA/TAPS detector. Within the Bonn-Gatchina partial wave analysis, the new polarization data lead to a significant narrowing of the error band for the multipoles for neutral-pion photoproduction.

Keywords: baryon spectroscopy, meson photoproduction, polarization observables, multipoles

1. Introduction

The measurement of the two double polarization observables G [1] and E [2] in photoproduction of neutral pions revealed significant differences between the data and the predictions from analyses such as MAID [3], SAID [4], and BnGa [5]. Partly, large discrepancies were observed even at rather low photon energies. This was surprising since the reaction $\gamma p \to p\pi^0$ is certainly the best studied photoproduction process. These discrepancies underline the importance of polarization observables for an interpretation of photoproduction data.

In this letter, we report a measurement of further polarization observables, called T, P, and H, for the reaction

$$\gamma p \to p\pi^0 . \tag{1}$$

All three observables were determined simultaneously from the same measurement and provide the next important step toward a better understanding of π^0 photoproduction. The target asymmetry T is a measure of the azimuthal asymmetry when the target nucleon carries polarization p_{T} in a direction perpendicular to the beam axis. P, often termed the recoil polarization observable, is a measure of the induced polarization of the recoiling nucleon. Here, P is determined from a double polarization measurement rather than from an experimentally more challenging direct measurement of the recoil polarization. This has the advantage that P can be determined in the very same measurement for almost the full solid angle, rather than by measuring P for specific points in angle and energy, as it has been done in the past. The observables P and H can be determined from azimuthal asymmetries using measurements with linearly polarized photons and transversely polarized target nucleons having polarization p_{T}. Part of the data presented here were used as a basis for an energy independent partial wave analysis (PWA) [6]. They are

now included in the BnGa PWA and multipoles for reaction (1) were determined. The multipoles were compared to those from MAID, SAID, Juelich2015 [7] and earlier BnGa PWA-solutions.

2. The experiment

The experiment was performed at the Bonn Electron Stretcher Accelerator ELSA [8]. Linearly polarized photons were produced by scattering a $3.2\,\mathrm{GeV}$ electron beam off a diamond crystal [9]. The crystal was oriented to position the coherent edge at $950\,\mathrm{MeV}$, leading to a polarization maximum of $p_\gamma = 65\%$ at $850\,\mathrm{MeV}$ which declined to 40% at $700\,\mathrm{MeV}$. Two perpendicular settings of the beam polarization plane were used (named $\parallel$ and $\perp$). Photon energies were measured in a tagging system described in Ref. [9].

The photon beam hits a butanol (C_4H_9OH) target with transversely polarized protons [10] with a mean proton polarization of $p_T \approx 75\%$. Data were taken with two opposite settings of the target polarization direction (named $\uparrow$ and $\downarrow$).

The incoming photons may produce a π^0 in the reaction (1). The neutral pions were reconstructed from their $\pi^0 \to 2\gamma$ decays in the Crystal Barrel (1320 CsI(Tl)-crystals) [11] and TAPS (216 BaF_2 crystals) [12, 13] electromagnetic calorimeters (see Fig. 1) which cover almost the full angular range down to $\theta = 1°$ in the forward direction. Protons from reaction (1) were detected in a three-layer cylindrical scintillation detector with 513 fibers [14] surrounding the target, in 180 small organic scintillators in front of 90 forward CsI(Tl) crystals covering the angular range from $27.5°$ to $11.2°$, and in organic scintillators mounted in front of each of the BaF_2 crystals. A CO_2 Cherenkov detector was installed in front of the BaF_2 crystals to identify background from electromagnetic reactions. The first-level trigger was derived from the tagger, the fiber detector, the forward calorimeters, and from the CO_2 Cherenkov detector as a veto; a second-level trigger used a FAst Cluster Encoder (FACE) [15] and selected events with at least two distinct calorimeter hits in the full detector assembly.

For further analysis only events with three distinct calorimeter hits were used. Adding events where only the two photons were measured would lead to an increased background contribution from other channels since several of the cuts discussed below can no longer be applied. For the events with three calorimeter hits, all three possible combinations were treated as $p\gamma\gamma$ candidates, with the proton being treated as a missing particle. Kinematic cuts were applied to ensure momentum conservation. Examples for the missing mass and azimuthal angle difference distributions are shown in Fig. 3. Energy- and angle-dependent $\pm 2\sigma$ cuts were applied based on the corresponding distributions. In addition, a $\pm 2\sigma$-cut on the polar-angle difference between the directions of the missing proton and the measured proton candidate was performed, and $\gamma p \to p\pi^0$
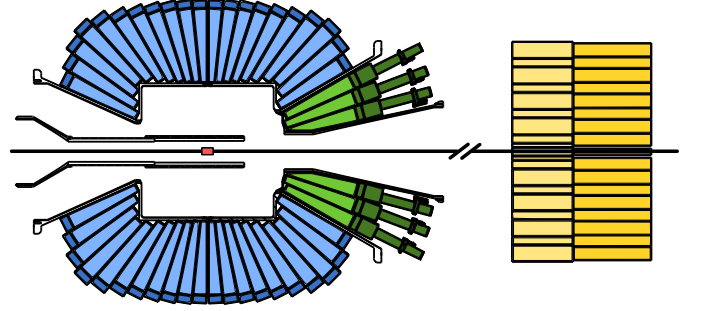

Figure 1: (Color online) The central part of the detector system. The 1320 CsI(Tl) crystals (blue and green) are read out via wavelength shifters and photodiodes (blue) or via photomultipliers (green), the 216 BaF_2 crystals (yellow) in forward direction are read out with photomultipliers. The target is surrounded by a 3-layer-scintillating fiber detector. To detect charged particles, scintillators are also placed in front of the forward CsI(Tl) (green) and TAPS crystals (yellow).
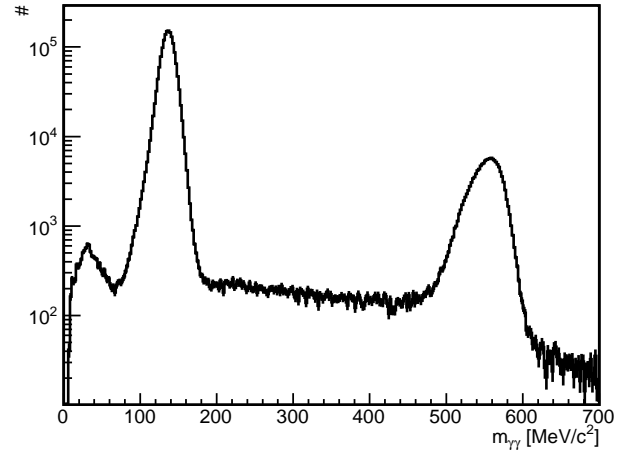

Figure 2: The invariant $\gamma\gamma$ mass distribution for the butanol data, after all cuts discussed (see text) have been applied. The final data sample of $p\pi^0$ events has a background contamination of less than 1%.

events were selected by a $\pm 2\sigma$ cut on the invariant $\gamma\gamma$ mass. Finally, a time coincidence was required between the tagger hit and the reaction products and a random-time background subtraction was performed. This resulted in a final data sample containing a total of 1.4 million $p\pi^0$ events. The background contamination was estimated from the invariant $\gamma\gamma$ mass spectrum (see Fig. 2), assuming a linear behaviour of the background under the peak. It is less than 1% for all energies and angles. The selected events for each of the four combinations of beam and target polarization directions were normalized to the corresponding photon flux and polarization degree for further analysis.

Since a butanol target was used, not only polarized and unpolarized free protons contributed to the count rates but also reactions occurring on the bound unpolarized nucleons of the carbon and oxygen nuclei. Additional measurements using a carbon foam target were performed to determine
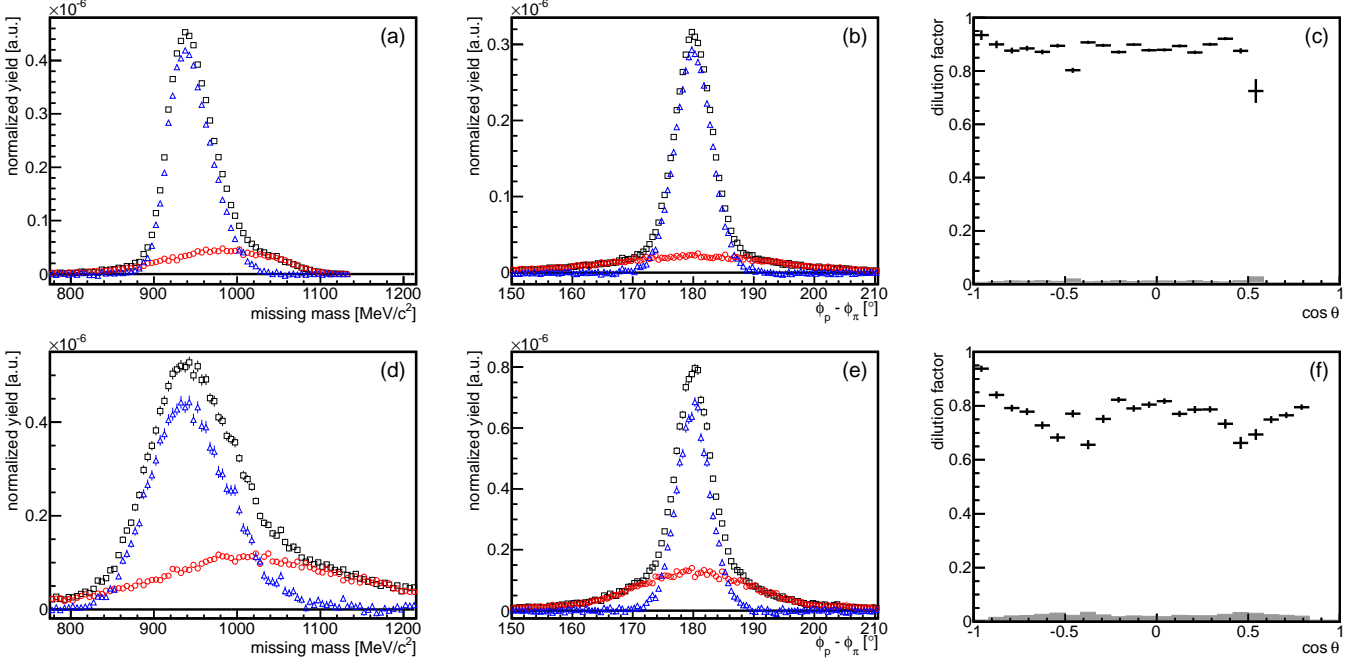
Figure 3: (Color online) (a,d) The missing mass distribution, with the proton as the missing particle, and (b,e) the azimuthal angle difference of π^0 and proton for reaction (1), for a γp invariant mass of $W = 1.46 - 1.48$ (top) and $1.82 - 1.94$ GeV (bottom); butanol ($\square$), scaled carbon ($\circ$), and the difference ($\triangle$). The distributions are shown after all other cuts discussed in the text are applied. From these distributions, the dilution factor (c,f) is determined. The gray band indicates the systematic uncertainty in the dilution factor due to uncertainties in the determination of the carbon scaling factor s. Since only events with all three particles detected in the calorimeter are considered an acceptance hole occurs for large $\cos(\theta)$. The observed structures in the dilution factor are due to a combined effect of reduced efficiencies for clusters impinging onto detector boundaries and Fermi smearing.

the so-called dilution factor $d(W, \cos\theta)$

$$
\begin{aligned}
d(W, \cos\theta) &= \frac{N_{\text{free}}(W, \cos\theta)}{N_{\text{butanol}}(W, \cos\theta)} \\
&= \frac{N_{\text{butanol}}(W, \cos\theta) - N_{\text{bound}}(W, \cos\theta)}{N_{\text{butanol}}(W, \cos\theta)}
\end{aligned} \quad (2)
$$

which assumes that the nucleons bound in carbon and oxygen show the same response to the impinging photons. The carbon foam target had the same size as the butanol target and approximately the same target area density as the carbon and oxygen part in the butanol. The carbon target replaced the butanol target in the frozen spin cryostat to match the experimental conditions of the butanol measurement as closely as possible. The flux-normalized carbon yield was compared to the flux-normalized butanol data using the distribution of the angle between the π^0 and proton in the azimuthal plane outside the region where contributions from free protons can be expected (see Fig. 3). Counting the yields for $|\Delta\phi - 180°| > 20°$, a global scaling factor $s = 1.13 \pm 0.01_{\text{stat.}} \pm 0.11_{\text{sys.}}$ was determined based on which the dilution factor (Eq. 2) was calculated using

$$
N_{\text{bound}}(W, \cos\theta) = s \cdot N_{\text{carbon}}(W, \cos\theta). \quad (3)
$$

Taking the slightly different densities of the butanol and carbon targets into account, one would expect a scaling

factor of $s \approx 1.1$, which is in agreement with the value obtained from the data. Energy- and angle-dependent deviations from the global scaling factor s were investigated by determining $s(W, \cos\theta)$ indepently for each bin and comparing it to the global value. The observed deviations are of the same magnitude as their statistical uncertainty. The global value is used, with the deviation contributing to the systematic uncertainty.

Figure 3 shows, for two energy bins, the azimuthal angle difference and the missing mass distributions of the butanol and scaled carbon data as well as their resulting difference. From these distributions the dilution factor as function of $\cos\theta$ for each energy bin was determined. The dilution factor is quite large, around 0.9 at low energies and decreasing to around 0.6 at higher energies. Note that a dilution factor $d = 1$ corresponds to non-existent carbon background and therefore to no dilution. The observed structures (Fig. 3) are due to a combined effect of reduced efficiencies for clusters impinging onto detector boundaries and Fermi smearing. They are reproduced in Monte Carlo simulations. At higher energies, the reduced missing mass resolution required a wider cut. Therefore the carbon contribution remaining after all cuts increased significantly, resulting in a smaller dilution factor.

3

3. The polarization observables

In the coordinate frame of the detector system, with α being the azimuthal angle of the photon beam polarization plane in the $\parallel$ setting, β the azimuthal angle of the target polarization vector in the $\uparrow$ setting, and ϕ the azimuthal angle of the produced π^0, the differential cross section can be written as

$$\frac{d\sigma}{d\Omega} = \left(\frac{d\sigma}{d\Omega}\right)_0 \cdot \{1 - p_\gamma \Sigma \cos(2(\alpha - \phi)) + p_{\mathrm{T}} T \sin(\beta - \phi)$$
$$- p_\gamma p_{\mathrm{T}} P \cos(2(\alpha - \phi)) \sin(\beta - \phi)$$
$$+ p_\gamma p_{\mathrm{T}} H \sin(2(\alpha - \phi)) \cos(\beta - \phi)\}. \qquad (4)$$

In a first step, the ordinary beam asymmetry Σ^{but} for each bin in energy and angle was determined:

$$\Delta N_{\mathrm{beam}}(\phi) = \frac{1}{p_\gamma} \cdot \frac{N_\perp - N_\parallel}{N_\perp + N_\parallel} = \Sigma^{\mathrm{but}} \cdot \cos(2(\alpha - \phi)). \quad (5)$$

A typical distribution is shown in Fig. 4a. The resulting beam asymmetries Σ^{but} agree very well with previously reported measurements [9, 16, 17] although the data sample contains in part reactions off nucleons of the C/O-nuclei. Results for Σ^{but} are not shown here.

To determine T, the asymmetry of the data sets with respect to the target polarization directions $\uparrow$ and $\downarrow$ was used, resulting in

$$\Delta N_{\mathrm{target}}(\phi) = \frac{1}{d\, p_{\mathrm{T}}} \cdot \frac{N_\uparrow - N_\downarrow}{N_\uparrow + N_\downarrow} = T \cdot \sin(\beta - \phi) \qquad (6)$$

with d given by Eq. 2. The target asymmetry was determined by a fit to the $\Delta N_{\mathrm{target}}(\phi)$ distributions as shown by the example in Fig. 4b. Figure 5 shows $\Delta N_{\mathrm{target}}(\phi)$ for three different angular bins ($W=1.82-1.94\,\mathrm{GeV}$). These distributions underline the strong dependence of T on the scattering angle θ.

P and H can be extracted from the data by considering the linear beam-polarization plane ($\parallel$ and $\perp$) in addition to the target polarization, leading to

$$\Delta N_{\mathrm{beam\text{-}target}}(\phi) = \frac{1}{d\, p_\gamma p_{\mathrm{T}}} \cdot \frac{(N_{\perp\uparrow} - N_{\perp\downarrow}) - (N_{\parallel\uparrow} - N_{\parallel\downarrow})}{(N_{\perp\uparrow} + N_{\perp\downarrow}) + (N_{\parallel\uparrow} + N_{\parallel\downarrow})}$$
$$= P \sin(\beta - \phi) \cos(2(\alpha - \phi))$$
$$+ H \cos(\beta - \phi) \sin(2(\alpha - \phi)) \qquad (7)$$

with average beam polarization p_γ and $\alpha = 45°$, the direction of the polarization plane in the $\parallel$ setting. Again, the observables could easily be determined by a fit to the $\Delta N_{\mathrm{beam\text{-}target}}(\phi)$ distributions, see Fig. 4c.

The $\Delta N(\phi)$ distributions were fitted for each bin in energy W and angle θ. The resulting confidence level (CL) distribution for the fits is flat with a distinct increase well below 0.1%, as can be seen in Fig. 6. This increase was traced to fits of distributions with very low statistics (due to a low cross section or low acceptance). These fits were very sensitive to background fluctuations. These data were excluded from further analysis by performing a CL-cut at 0.1%.

The data on T, P, and H as functions of center-of-mass energy W and angle $\cos\theta$ are shown in Figs. 7–9. All observables exhibit a strong angular dependence which also changes significantly with W. The systematic uncertainty shown includes the uncertainty in the degree of photon (4%) and proton (2%) polarizations, in the dilution factor (1%–4%), and an additional absolute uncertainty (0.01) due to the remaining background contribution. For further details on the estimation of the systematic uncertainties see Refs. [9, 10, 18].

The polarization observable P describes the polarization of the outgoing proton in the direction perpendicular to the scattering plane. Here, it was determined indirectly from the correlation of beam and target polarization. Thus, both observables, P and H, were measured only in the energy region in which the photon beam carried a significant linear polarization; the results are hence restricted to the 665 to 930 MeV photon energy range. The target asymmetry T, shown in Fig. 7, does not require polarized photons, and the data allowed us to determine T up to $E_\gamma = 1900\,\mathrm{MeV}$. Above this energy, the count rates were small, and we do not present those results here.

The new data agree well with previously reported measurements of P [19] and T [20] but exceed the old data in precision and coverage in angles and energy. For H no earlier data exist in this energy range, the older data [21] are limited to $E_\gamma > 1300\,\mathrm{MeV}$. Our data up to 930 MeV were used as a basis for an energy independent PWA [6]. The high energy T-data are presented here for the first time. The new data sets have been included in the BnGa-PWA as discussed in the following.

4. Partial wave analysis

The data were fitted within the BnGa multi-channel partial wave analysis. Compared to our solutions BnGa2011-01 and BnGa2011-02, further data were included [1, 2, 25]. Relevant for the $\gamma p \to p\pi^0$ multipoles are the new data on T, P, and H as well as our recently published data on G [1] and on E [2]. Figures 10 and 11 compare the newly determined multipoles with those of BnGa2011-01 and BnGa2011-02. The error bands for the BnGa2011 solutions were derived from the (1σ) spread of 12 different solutions with different assumptions on the ingredients: the number of poles in the $J^P = 3/2^+$ wave was 3 or 4, in the $J^P = 5/2^+$ wave 2 or 3, the $N(1700)3/2^-$ width of the pole converged to a wide ($\sim$600 MeV) or a narrow ($\sim$250 MeV) value, a K-matrix formalism was used or, alternatively, an N/D-parametrization [23]. The χ^2 ranged from its minimum $\chi^2_{\min}$ to $\chi^2_{\min} + 800$. (Note that the absolute χ^2 value is meaningless since part of the data are multiparticle final states and fitted in an event-based likelihood fit. The log likelihood value is then converted into a pseudo-χ^2 [5].)
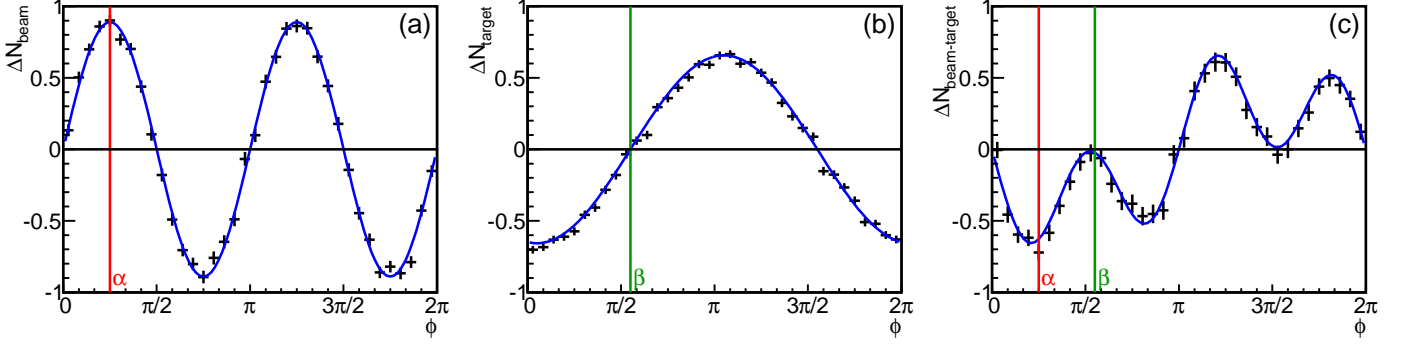
4

Figure 4: (Color online) Yield asymmetries as a function of ϕ for the energy bin $1.46\,\mathrm{GeV} < W < 1.48\,\mathrm{GeV}$. (a) $\Delta N_{\mathrm{beam}}(\phi)$, (b) $\Delta N_{\mathrm{target}}(\phi)$, (c) $\Delta N_{\mathrm{beam\text{-}target}}(\phi)$ fitted by the function of Eq. (5), Eq. (6), and Eq. (7), respectively.
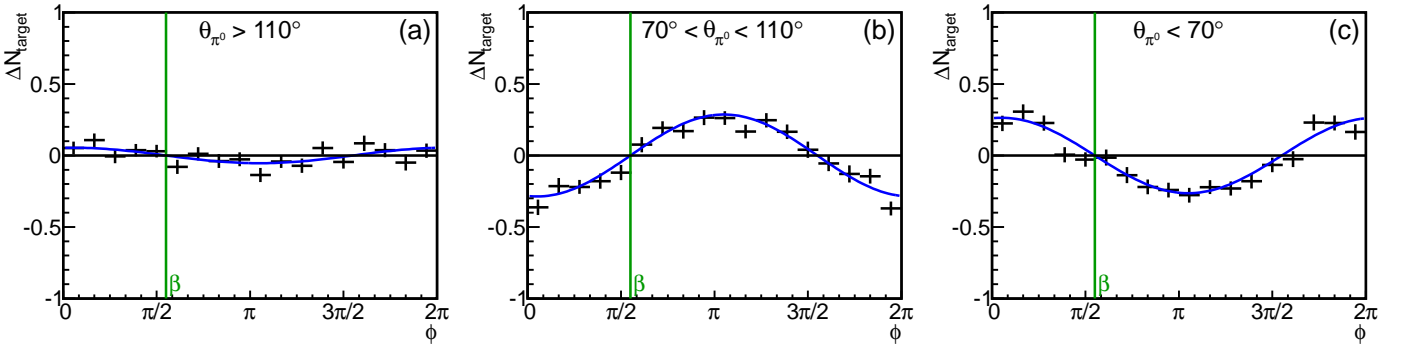

Figure 5: (Color online) Yield asymmetry $\Delta N_{\mathrm{target}}$ as a function of ϕ for three angular bins in θ in the γp invariant mass window $1.82\,\mathrm{GeV} < W < 1.94\,\mathrm{GeV}$.

In the new fits, we started from the same solutions and re-optimized all parameters. All fits converged, but 6 fits resulted in a χ^2 larger than the new χ^2-minimum ($\chi^2_{\mathrm{new\,min}}$) by 1000 units or more. These fits, mostly those with only 3 poles in the $J^P = 3/2^+$ wave, were then removed from the error analysis. The resulting error bands for all remaining solutions within $\chi^2_{\mathrm{new\,min}} + 800$ are also shown in Figs. 10 and 11. The χ^2-range for the new solutions was chosen consistently with the BnGa2011 solutions for which the multipoles have first been shown in [24].

The new error bands are significantly smaller than the previous ones. Averaged over all multipoles and energies, the errors are reduced by a factor of 2.25. Examples for multipoles which are substantially better defined are the M_1^- multipole to which the Roper resonance and $N(1710)1/2^-$ contribute and the M_2^+ multipole to which the $J^P = 5/2^-$-resonances contribute. In most cases, the old error bars cover the range of new solutions, the solutions are at least compatible with each other at the 2σ level over the full mass range.

There are few changes to the multipoles only: The E_1^+ multipole leading to the excitation of N and Δ resonances with $J^P = 3/2^+$ has kept its structure but its imaginary part has increased in strength in the fourth resonance region. Similar changes are also visible in the real part. The real part of the M_2^+ multipole ($J^P = 5/2^-$) has become smaller in absolute value in the $W = 1500\,MeV$ region,

while in the imaginary part changes are observed in the high mass region around $W = 2100\,MeV$. In all cases, where discrepancies with the MAID and SAID solutions were observed, these discrepancies remain while the consistency between BnGa2011 and BnGa2014 is rather good. The multipoles from Juelich2015 [7] show also significant differences compared to BnGa2014.

Summarizing, we have reported a simultaneous measurement of the polarization observables T, P, and H. With the data presented here an additional step toward a complete experiment in π^0-photoproduction off the proton has been made. The data provide a more precise determination of the photoproduction multipoles governing the photoproduction of single neutral pions off protons.

Acknowledgement

References

[1] A. Thiel *et al.*, Phys. Rev. Lett. **109**, 102001 (2012).
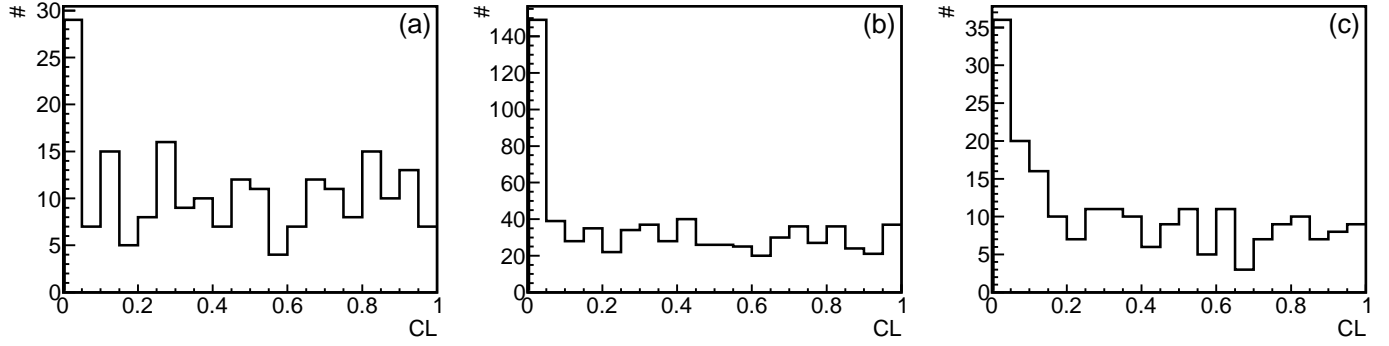   R.L. Workman, M.W. Paris, W.J. Briscoe, and I.I. Strakovsky,

Figure 6: Histograms of the confidence level of the fits to the (a) $\Delta N_{\text{beam}}(\phi)$, (b) $\Delta N_{\text{target}}(\phi)$, and (c) $\Delta N_{\text{beam-target}}(\phi)$ distributions. The increase of the CL in the first bin can be eliminated by requiring CL > 0.001.

Phys. Rev. Lett. **110**, 169101 (2013);
A. Thiel *et al.*, Phys. Rev. Lett. **110**, 169102 (2013).

[2] M. Gottschall *et al.*, Phys. Rev. Lett. **112**, 012003 (2014).

[3] D. Drechsel, S. S. Kamalov and L. Tiator, Eur. Phys. J. A **34**, 69 (2007).

[4] R. L. Workman *et al.*, Phys. Rev. C **85**, 025201 (2012).

[5] A. V. Anisovich, R. Beck, E. Klempt, V. A. Nikonov, A. V. Sarantsev and U. Thoma, Eur. Phys. J. A **48**, 15 (2012).

[6] J. Hartmann, H. Dutz *et al.*, Phys. Rev. Lett. **113**, 062001 (2014).

[7] D. Rönchen *et al.*, arXiv:1504.01643 [nucl-th].

[8] W. Hillert, Eur. Phys. J. A **28S1**, 139 (2006).

[9] D. Elsner *et al.*, Eur. Phys. J. A **39**, 373 (2009).

[10] Ch. Bradtke, H. Dutz, H. Peschel *et al.*, Nucl. Instrum. Meth. M A **436**, 430 (1999).

[11] E. Aker *et al.*, Nucl. Instrum. Meth. A **321**, 69 (1992).

[12] R. Novotny *et al.*, IEEE Trans. Nucl. Sci. **38**, 379 (1991).

[13] A.R. Gabler *et al.*, Nucl. Instrum. Meth. A **346**, 168 (1994).

[14] G. Suft *et al.*, Nucl. Instrum. Meth. A **538**, 416 (2005).

[15] H. Flemming, doctoral thesis, University of Bochum (2001).

[16] O. Bartalini *et al.*, Eur. Phys. J. A **26**, 399 (2005).

[17] N. Sparks *et al.*, Phys. Rev. C **81**, 065210 (2010).

[18] J. Hartmann, doctoral thesis in preparation, University of Bonn (2015).

[19] V.G. Gorbenko *et al.*, Pisma Zh. Eksp. Teor. Fiz. **19**, 659 (1974).
V.G. Gorbenko *et al.*, Yad. Fiz. **27**, 1204 (1978).
A.A. Belyaev *et al.*, Nucl. Phys. B **213**, 201 (1983).
J.O. Maloy, Ph.D. Thesis, 1961. 141pp.
V.G. Gorbenko *et al.*, Pisma Zh. Eksp. Teor. Fiz. **22**, 393 (1975).
P.J. Bussey *et al.*, Nucl. Phys. B **154**, 492 (1979).
S. Kato *et al.*, Nucl. Phys. B **168**, 1 (1980).
A.S. Bratashevsky *et al.*, Nucl. Phys. B **166**, 525 (1980).
A.S. Bratashevsky *et al.*, Ukr. Fiz. Zh. (Russ.Ed.) **31**, 1306 (1986).

[20] V.G. Gorbenko *et al.*, Pisma Zh. Eksp. Teor. Fiz. **19**, 659 (1974).
V.G. Gorbenko *et al.*, Yad. Fiz. **27**, 1204 (1978).
P.S.L. Booth *et al.*, Nucl. Phys. B **121**, 45 (1977).
P. Feller *et al.*, Nucl. Phys. B **110**, 397 (1976).
V.G. Gorbenko *et al.*, Yad. Fiz. **26**, 320 (1977).
H. Herr *et al.*, Nucl. Phys. B **125**, 157 (1977).
M. Fukushima *et al.*, Nucl. Phys. B **136**, 189 (1978).
P.J. Bussey *et al.*, Nucl. Phys. B **154**, 492 (1979).
K.S. Agababian *et al.*, Yad. Fiz. **50**, 1341 (1989).
M.M. Asaturian *et al.*, JETP Lett. **44**, 341 (1986).
A. Bock *et al.*, Phys. Rev. Lett. **81**, 534 (1998).
J.O. Maloy, Ph.D. Thesis, 1961. 141pp.

[21] P.J. Bussey *et al.*, Nucl. Phys. B **159**, 383 (1979).

[22] R. L. Workman *et al.*, M. W. Paris, W. J. Briscoe and I. I. Strakovsky, Phys. Rev. C **86**, 015202 (2012).

[23] A. Sarantsev, "N/D-based method for the analysis of meson production data" (in preparation).

[24] A. V. Anisovich, R. Beck, E. Klempt, V. A. Nikonov, A. V. Sarantsev and U. Thoma, Eur. Phys. J. A **48**, 88 (2012).

[25] E. Gutz *et al.*, Eur. Phys. J. A **50**, 74 (2014)
V. Sokhoyan *et al.*, "High statistics study of the reaction $\gamma p \to p \, 2\pi^0$" in preparation.
V. Sokhoyan *et al.*, Phys. Lett. B746 (2015) 127.
V. L. Kashevarov *et al.*, Phys. Rev. C **85**, 064610 (2012).
M. L. Good and R. R. Kofler, Phys. Rev. **183**, 1142 (1969).
J. C. Doyle, F. S. Crawford and J. A. Anderson, Phys. Rev. **165**, 1483 (1968).
O. I. Dahl *et al.*, Phys. Rev. **163**, 1430 (1967) [Erratum-ibid. **183**, 1520 (1969)].
O. Goussu *et al.*, Nuovo Cim. A **42**, 606 (1966).
T. C. Jude *et al.*, Phys. Lett. B **735**, 112 (2014).
R. D. Baker *et al.*, Nucl. Phys. B **145**, 402 (1978).
T. O. Binford *et al.*, Phys. Rev. **183**, 1134 (1969).
O. I. Dahl *et al.*, Phys. Rev. **163**, 1430 (1967) [Erratum-ibid. **183**, 1520 (1969)].
L. L. Yoder *et al.*, Phys. Rev. **132**, 1778 (1963).
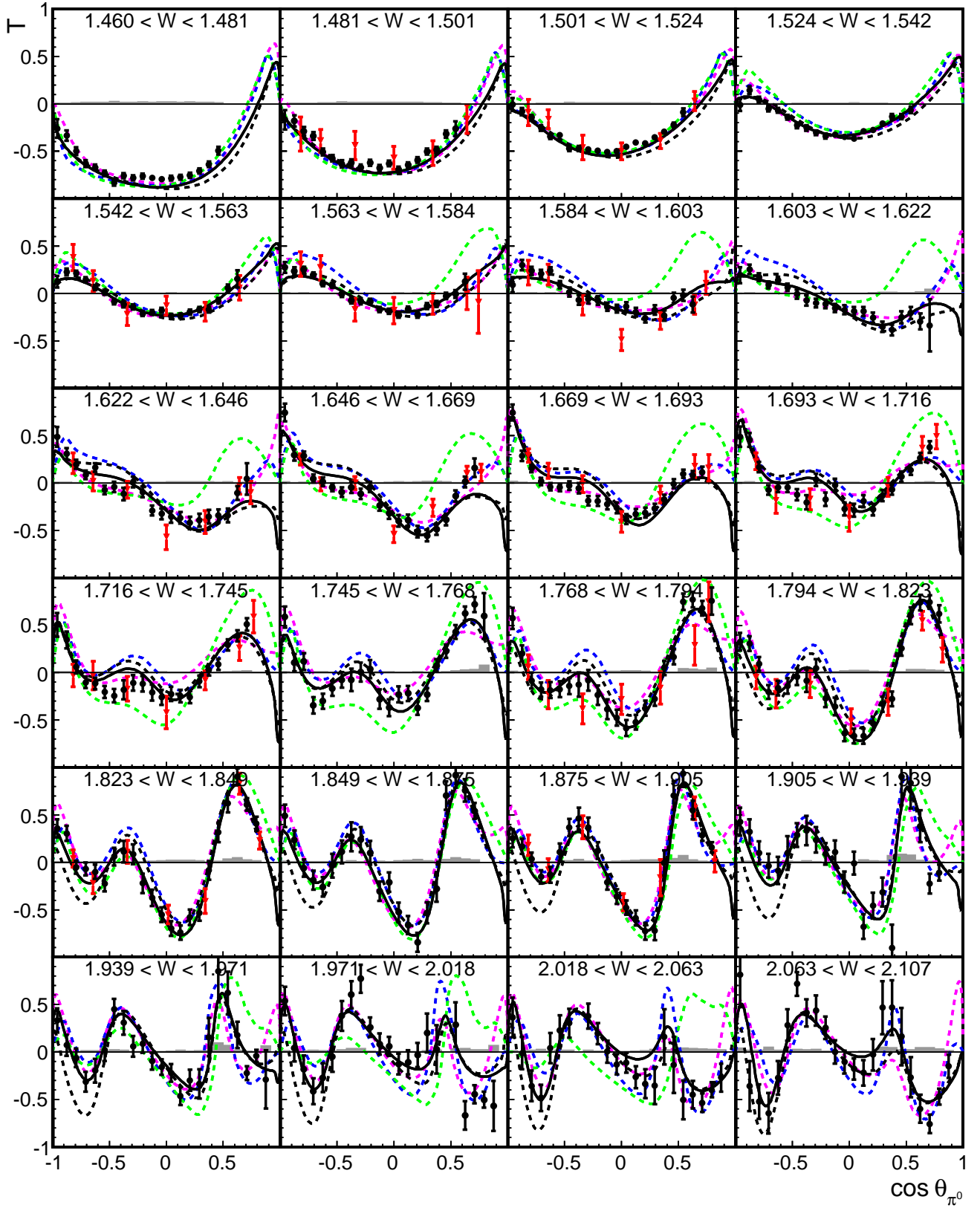P. Aguar-Bartolome *et al.*, Phys. Rev. C **88**, no. 4, 044601 (2013).

Figure 7: (Color online) The polarization observable T as function of the γp invariant mass W (in GeV) and of the scattering angle $\cos\theta$. The systematic uncertainty is shown as dark gray band. An additional systematic uncertainty on the photon energy (from $\sigma_{E_\gamma}^{\mathrm{sys}} = 6.5$ MeV at the lowest to 2.3 MeV at the highest energy bin) is not shown. The low energy data were presented in [6]. Earlier data (gray, (red, online)) are from [20]. The solid line represents our best fit BnGa2014. The data are compared to predicitions (dashed curves) from BnGa2011-02 (black), MAID [3] (light gray, (green, online)), SAID CM12 [22] (dark gray, (blue, online)), and Juelich2015 [7] (gray, (magenta, online)).
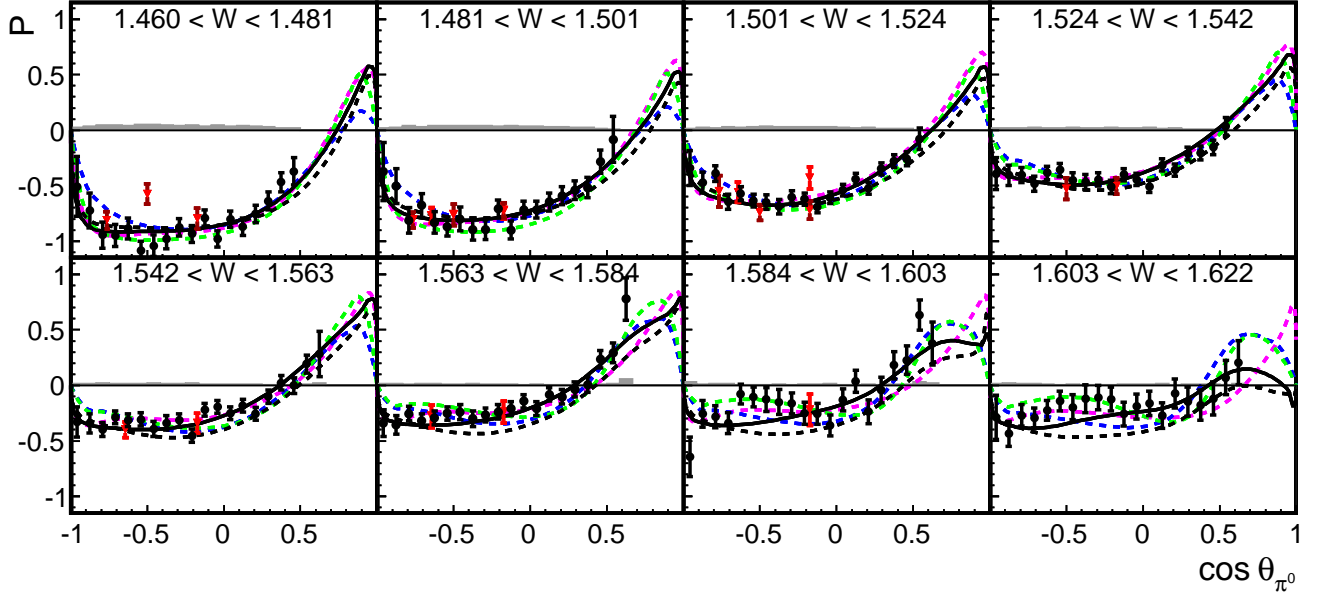
Figure 8: (Color online) The polarization observable P [6] as functions of the γp invariant mass W (in GeV) and of the scattering angle $\cos\theta$. The systematic uncertainty is shown as dark gray band. An additional systematic uncertainty on the photon energy (from $\sigma^{\mathrm{sys}}_{E_\gamma} = 6.5$ MeV at the lowest to 5.4 MeV at the highest energy bin) is not shown. Earlier data (gray, (red, online)) are from [19]. The solid line represents our best fit BnGa2014. The data are compared to predictions (dashed curves) from BnGa2011-02 (black), MAID [3] (light gray, (green, online)), SAID CM12 [22] (dark gray, (blue, online)), and Juelich2015 [7] (gray, (magenta, online)).
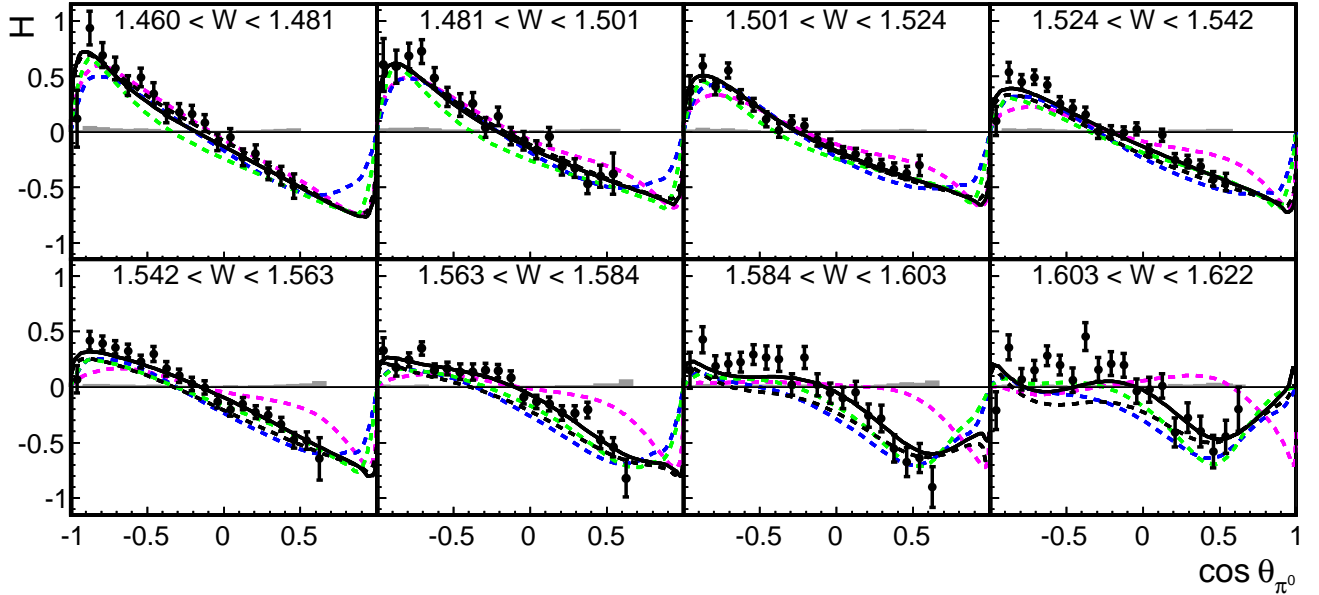

Figure 9: (Color online) The polarization observable H [6] as functions of the γp invariant mass W (in GeV) and of the scattering angle $\cos\theta$. The systematic uncertainty is shown as dark gray band. An additional systematic uncertainty on the photon energy (from $\sigma^{\mathrm{sys}}_{E_\gamma} = 6.5$ MeV at the lowest to 5.4 MeV at the highest energy bin) is not shown. The solid line represents our best fit BnGa2014. The data are compared to predictions (dashed curves) from BnGa2011-02 (black), MAID [3] (light gray, (green, online)), SAID CM12 [22] (dark gray, (blue, online)), and Juelich2015 [7] (gray, (magenta, online)).
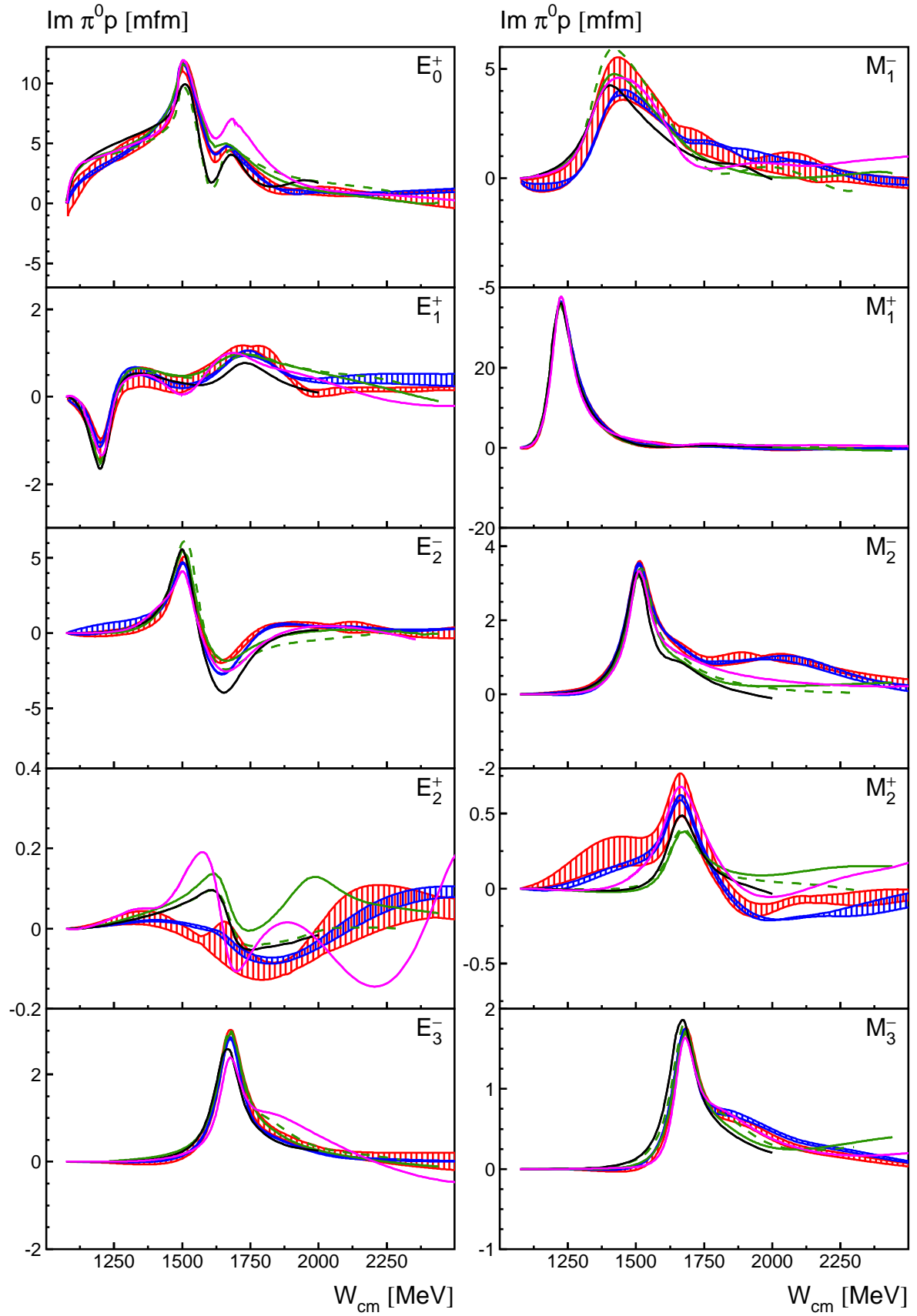
Figure 10: (Color online) Multipole decomposition of the $\gamma p \to p\pi^0$ transition amplitudes, imaginary part. The light (red) shaded areas give the range from a variety of different fits derived from solution BnGa2011-01 and BnGa2011-02 [5]. The dark (blue) shaded area represents the range of solutions when the new data are included in the fit. The black curves represent the MAID fit [3], the light (green) solid curves SAID-CM12 [22], the light (green) dashed curves SAID-SN11 [4], and the magenta curve the Juelich2015 [7] solution. For the BnGa-multipoles an error band (see text) has been determined. Such an error band is presently not provided by the other analyses.
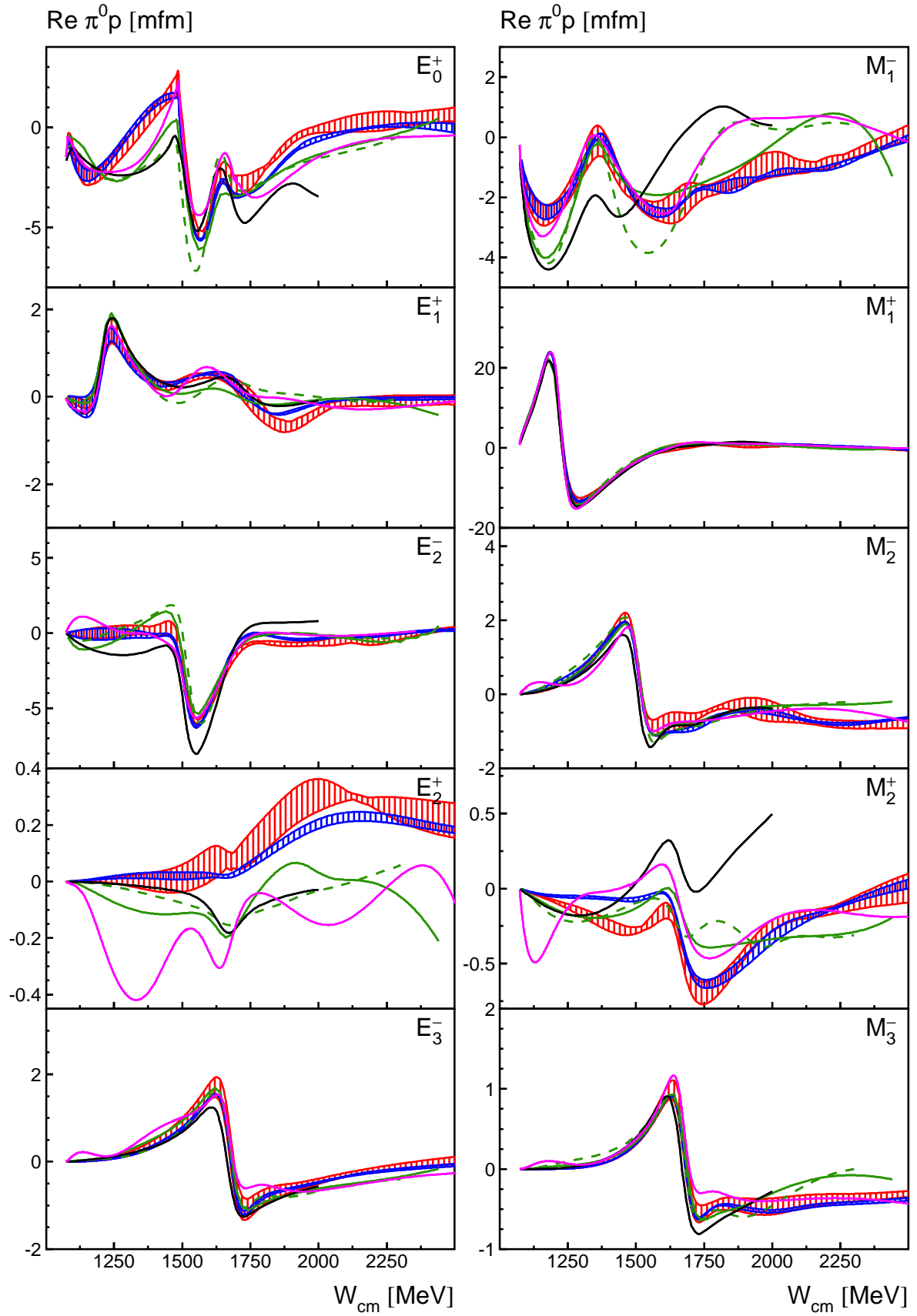
Figure 11: (Color online) Multipole decomposition of the $\gamma p \to p\pi^0$ transition amplitudes, real part. The light (red) shaded areas give the range from a variety of different fits derived from solution BnGa2011-01 and BnGa2011-02 [5]. The dark (blue) shaded area represents the range of solutions when the new data are included in the fit. The black curves represent the MAID fit [3], the light (green) solid curves SAID-CM12 [22], the light (green) dashed curves SAID-SN11 [4], and the magenta curve the Juelich2015 [7] solution. For the BnGa-multipoles an error band (see text) has been determined. Such an error band is presently not provided by other analyses.